Narrow-Band Least-Squares Infrasound Array Processing

Alexandra M. lezzi*16, Robin S. Matoza16, Jordan W. Bishop2,36, Sneha Bhetanabhotla¹, and David Fee^{2,4}

Abstract

Infrasound data from arrays can be used to detect, locate, and quantify a variety of natural and anthropogenic sources from local to remote distances. However, many array processing methods use a single broad frequency range to process the data, which can lead to signals of interest being missed due to the choice of frequency limits or simultaneous clutter sources. We introduce a new open-source Python code that processes infrasound array data in multiple sequential narrow frequency bands using the least-squares approach. We test our algorithm on a few examples of natural sources (volcanic eruptions, mass movements, and bolides) for a variety of array configurations. Our method reduces the need to choose frequency limits for processing, which may result in missed signals, and it is parallelized to decrease the computational burden. Improvements of our narrow-band least-squares algorithm over broad-band leastsquares processing include the ability to distinguish between multiple simultaneous sources if distinct in their frequency content (e.g., microbarom or surf vs. volcanic eruption), the ability to track changes in frequency content of a signal through time, and a decreased need to fine-tune frequency limits for processing. We incorporate a measure of planarity of the wavefield across the array (sigma tau, σ_{τ}) as well as the ability to utilize the robust least trimmed squares algorithm to improve signal processing and insight into array performance. Our implementation allows for more detailed characterization of infrasound signals recorded at arrays that can improve monitoring and enhance research capabilities.

Cite this article as lezzi, A. M., R. S. Matoza, J. W. Bishop, S. Bhetanabhotla, and D. Fee (2022). Narrow-Band Least-Squares Infrasound Array Processing, Seismol. Res. Lett. XX, 1-16, doi: 10.1785/0220220042.

Introduction

Infrasound (sound waves below 20 Hz) can be recorded from a variety of natural and anthropogenic sources. Sensors are often deployed as arrays, or groups of sensors in a given configuration, that can enhance the ability to detect and distinguish coherent infrasound signals from background noise. This is typically done by the time difference of arrival of a signal at the various elements of the array, assuming a plane wave crossing the array. Infrasound arrays can be located at a variety of distances from the source, including local (\leq 15 km), regional (\sim 15–250 km), and remote distances (≥250 km) (Fee and Matoza, 2013; Matoza et al., 2018). The International Monitoring System (IMS) aims to detect and locate potential nuclear explosion testing, and includes a global network of 60 planned infrasound arrays (53 of which have been installed as of 2021; Christie and Campus, 2010). These IMS arrays have been used to research a variety of other sources of infrasound, including volcanic eruptions (e.g., Matoza et al., 2017), chemical explosions (e.g., Fee et al., 2013), microbaroms (e.g., Le Pichon et al., 2006; Landès et al., 2012), and bolides (e.g., Le Pichon et al., 2013; Pilger et al., 2015; Arrowsmith et al., 2021). In addition to this

global network of infrasound arrays, many regional infrasound arrays exist, such as those operated by the Alaska Volcano Observatory (AVO; e.g., Lyons et al., 2020).

Common infrasound array processing methods include progressive multi-channel correlation (PMCC; e.g., Cansi, 1995; Cansi and Klinger, 1997), frequency-wavenumber analysis (e.g., Smart and Flinn, 1971), and least-squares beamforming (e.g., Szuberla and Olson, 2004; Olson and Szuberla, 2005), as well as a variety of others. Aside from PMCC, many array processing methods use a single broad frequency band for processing, which often requires "fine tuning" (manual selection) of the frequency limits to best enhance signal detection

^{1.} Department of Earth Science and Earth Research Institute, University of California, Santa Barbara, California, U.S.A., https://orcid.org/0000-0002-6782-7681 (AMI); https://orcid.org/0000-0003-4001-061X (RSM); 2. Wilson Alaska Technical Center, Geophysical Institute, University of Alaska Fairbanks, Fairbanks, Alaska, U.S.A., (b) https://orcid.org/0000-0002-8940-9827 (JWB); (b) https://orcid.org/0000-0002-0936-9977 (DF); 3. Earth & Environmental Sciences Division, Los Alamos National Laboratory, Los Alamos, New Mexico, U.S.A.: 4. Alaska Volcano Observatory. Geophysical Institute, University of Alaska Fairbanks, Fairbanks, Alaska, U.S.A. *Corresponding author: amiezzi@ucsb.edu

[©] Seismological Society of America

while diminishing the detection of clutter sources (infrasound sources other than the signal of interest). PMCC is the main array processing tool used by the International Data Centre to process data from the IMS arrays (Cansi, 1995; Cansi and Klinger, 1997; Mialle *et al.*, 2019). The least-squares array processing method and mean cross-correlation maxima (MCCM) metric (Szuberla and Olson, 2004; Olson and Szuberla, 2005; Wilson *et al.*, 2009; Lee *et al.*, 2013; Bishop *et al.*, 2020) are also popular for operational usage (e.g., De Angelis *et al.*, 2012; Lyons *et al.*, 2020; Shiro *et al.*, 2021), including at the U.S. Geological Survey Alaska Volcano Observatory, Cascades Volcano Observatory, Hawaiian Volcano Observatory, and Volcano Disaster Assistance Program.

Least-squares array processing is well established, opensource (e.g., Bishop et al., 2020), and easy to understand with statistical uncertainty. The least-squares processing repository used in Bishop et al. (2020) can analyze any data that can be read into Python, including from a variety of servers (e.g., the Incorporated Research Institutions for Seismology [IRIS]) or from locally stored data (e.g., miniseed, Seismic Analysis Code [SAC], and other common data formats), making it an approachable array processing method. Although least-squares processing appears to be a useful method, there are some limitations to using this processing method in its typical implementation. In its ordinary application, this approach can sometimes miss signals of interest, such as explosions or volcanic signals, due to other sources, such as the microbarom or surf, being present in the same processing band. Because least-squares array processing is typically applied in a single broad frequency band, the results are sensitive to processing parameters such as frequency limits (e.g., Schwaiger et al., 2020), and there is little information provided about the frequency content of the source, including if it is changing through time. We show that these limitations of the broad-band least-squares processing can be mitigated by performing least-squares processing in multiple sequential narrow frequency bands. Improvements of the multiple narrow band processing over broad-band least squares include: (1) improved ability to distinguish between multiple sources with different frequency content such as the microbarom and/or surf from signals of interest, (2) more accurate representation of event duration, (3) enhanced signal detection capabilities, (4) improved ability to illuminate changes in frequency content within a signal, (5) upgraded capability to distinguish between multiple simultaneous sources if distinct in their frequency content, and (6) does not require "fine tuning" of frequency limits based on individual array and signal characteristics.

In this study, we describe our implementation of narrowband least-squares array processing for infrasound data, introduce our open-source Python code with relevant processing parameters, and investigate our new implementation for a few examples. We find that performing least-squares array processing in multiple sequential narrow frequency bands improves array processing results and therefore the detection capabilities compared to typical broad-band least-squares array processing. This implementation allows for more detailed characterization of the signal characteristics (e.g., ability to observe changes in frequency content) that can improve monitoring and enhance research capabilities.

Algorithm and Capabilities

Least-squares beamforming (the process in which traces from each element in an array are aligned in time for a given slowness value in a least-squares sense) is a common method for infrasound array processing, both for research and monitoring purposes. We assume an infrasonic signal that propagates as a plane wave across the array of n elements and N element pairs, which is typically valid for sources far from the array (Szuberla et al., 2006). Least-squares regression of interelement travel times over interelement distances can be used to estimate the optimal slowness vector $\boldsymbol{\beta}$ of the propagating signal over successive time windows with a given window length and overlap

$$\boldsymbol{\beta} = (\beta_x, \beta_y)^T = \frac{\mathbf{k}}{\omega},\tag{1}$$

in which **k** is the wavenumber of the propagating wave, and ω is the angular frequency. The $N \times 1$ vector of interelement travel time differences (τ) can be expressed as (e.g., Szuberla and Olson, 2004; Bishop *et al.*, 2020):

$$\tau = \mathbf{A}\boldsymbol{\beta} + \boldsymbol{\epsilon},\tag{2}$$

in which **A** is the $N \times 2$ matrix of co-array coordinates (interelement distances), and ϵ is the $N \times 1$ vector of measurement errors. This system of equations is solved by minimizing the sum of the squared residuals:

$$\hat{\boldsymbol{\beta}} = \frac{\text{minimize}}{\boldsymbol{\beta}} \sum_{i=1}^{N} |r_i(\boldsymbol{\beta})|^2, \tag{3}$$

in which r_i is the *i*th component of the residual vector, $r = A\beta - \tau$. Under the assumption that the errors in estimating the interelement travel times are normally distributed, then the least-squares (L_2 norm) solution is the maximum-likelihood solution (Montgomery *et al.*, 2001).

From the estimation of the slowness vector, the back azimuth (θ is the direction of arrival defined here as clockwise from north) and trace velocity (ν is the speed in the plane of the array) can be computed as follows:

$$\theta = \tan^{-1} \left(\frac{\beta_x}{\beta_y} \right), \tag{4}$$

$$\nu = \frac{1}{\sqrt{\beta_x^2 + \beta_y^2}} = \frac{1}{||\beta||}.$$
 (5)

We use the maximum of the normalized cross-correlation function between array elements to estimate the travel times between the element pairs in the array, termed the MCCM. Recently, some authors have switched from MCCM (e.g., Haney *et al.*, 2018; Iezzi *et al.*, 2019; Lyons *et al.*, 2020) to median cross-correlation maxima (MdCCM; e.g., Gabrielson, 2017; Bishop *et al.*, 2020), as the median value is more resistant to outliers. We note that many other metrics for detection are in use, including the time domain Fisher analysis (Blandford, 1974) and frequency domain *F*-statistic analysis (Shumway, 1971; Smart and Flinn, 1971). An estimate of the standard deviation of the time delays, termed sigma tau (σ_{τ}), can be used as an indicator of nonplanar propagation across the array (Szuberla *et al.*, 2006). The σ_{τ} is defined as:

$$\sigma_{\tau} = \sqrt{\frac{\boldsymbol{\tau}^T (\boldsymbol{I} - \mathbf{A} (\mathbf{A}^T \mathbf{A})^{-1} \mathbf{A}^T) \boldsymbol{\tau}}{N - 2}},$$
 (6)

in which **I** is the $N \times N$ identity matrix. Here we have assumed that A has a rank of 2 (Szuberla and Olson, 2004). Another interpretation of σ_{τ} is that it is a scaled residual vector magnitude, so interelement time delays that are not well described by the plane wave model lead to a larger σ_{τ} . Bishop et al. (2020) explore improvements to infrasound array processing using robust statistical estimators. The least trimmed squares (LTS) estimator allows for individual element pairs to be automatically dropped from processing that produce outlying travel times, which can be viewed as violating the plane wave assumption. Thus, Bishop et al. (2020) find that the LTS implementation of the least-squares algorithm provides robust array processing results and insight into array performance (e.g., timing errors and sensor issues). Further discussion on the statistical confidence or uncertainty in the estimation of direction of arrival (back azimuth) and trace velocity are described by Szuberla and Olson (2004) and De Angelis et al. (2020).

We perform least-squares array processing separately on multiple sequential narrow frequency bands and consolidate the results to improve signal detection and time-frequency characterization. Our Python code is openly available on Github and relies upon another openly accessible repository for least-squares array processing. We emphasize flexibility in this implementation to allow the user to select the time and frequency parameters. The overall minimum (FMIN) and maximum (FMAX) frequencies are specified along with the number of narrow bands (NBANDS) between the two values. The narrow frequency bands can be specified with a variety of spacing options (FREQ_BAND_TYPE), including linear, logarithmic (e.g., Brachet et al., 2010), one octave, onethird octave (e.g., Garces, 2013), two overlapping octave (e.g., Green and Bowers, 2010), and user specified. The corresponding window lengths for each narrow band can be specified (WINDOW_LENGTH_TYPE) as either constant or adaptive (e.g., Brachet *et al.*, 2010; Le Pichon *et al.*, 2010), in which adaptive varies linearly with frequency. The filter type (FILTER_TYPE) can be specified as either Type I Chebyshev or Butterworth options. Typical least-squares in narrow bands is performed (ALPHA = 1.0), with the option of the LTS implementation of Bishop *et al.* (2020) (0.5 ≤ ALPHA < 1.0). The narrow-band least-squares code is parallelized to allow for the possibility of using this implementation on a similar timescale to broad-band least-squares, including near real-time monitoring. The parallelization is currently set to loop over the separate bands (parameter NBANDS). A full list of the parameters is included in the Appendix, and the impact of processing parameters is briefly explored in the Processing Parameter Investigation and Discussion section.

Example Usage and Applications

We investigate our narrow-band least-squares processing method on a few examples of natural sources for a variety of array configurations (e.g., four elements with a small aperture as well as more elements with a larger aperture). The broad-band least-squares array processing method is compared to our narrow-band least-squares implementation for each example, highlighting improvements in data processing and detection capabilities. The frequency limits for the broad-band least-squares processing for each example change according to those used in monitoring applications while the narrow-band least-squares implementation is consistent between examples (with two different band configurations used). A second order Type I Chebyshev filter with a ripple of 0.01 is used for all examples, and processing parameters are summarized in Table 1.

Eruption of Mount St. Helens, Washington

As part of the Acoustic Surveillance for Hazardous Eruptions (ASHE) project, an infrasound array was deployed in 2004 at Mount St. Helens, Washington, United States, which captured multiple explosive eruptions (Matoza *et al.*, 2007), including the 08 March 2005 (09 March UTC) phreatic eruption. The Coldwater (CDWR) array was located 13 km from the summit (back azimuth of 153°) and consisted of four MB2000 (DASE/Tekelec) broad-band aneroid microbarometers arranged in a centered triangle with an aperture of ~100 m (Fig. 1f) and porous hose wind noise suppression (Hedlin *et al.*, 2003). The data were sampled at 40 Hz and have a flat response from 0.01 to 17 Hz. We refer the reader to Matoza *et al.* (2007) for details on the array setup, eruption, and infrasound data analysis.

Least-squares array processing, both broad- and narrow-band, is applied to the CDWR data for the 09 March 2005 eruption using parameters that are similar to those used for PMCC by Matoza *et al.* (2007) (their fig. 9). The broad-band least-squares array processing uses a bandpass filter between

TABLE 1

Details for the Processing Parameters Used in the Examples, Including Band Number, Minimum and Maximum Frequency, Window Length, and Figure Number

Example	Band	Minimum Frequency (Hz)	Maximum Frequency (Hz)	Window Length (s)	Figure
Mount St. Helens	1	0.1	10.0	50	1a–d
Multiweek	1	1.0	1.5	30	2
	2	1.5	2.0	30	
	3	2.0	2.5	30	
	4	2.5	3.0	30	
	5	3.0	3.5	30	
	6	3.5	4.0	30	
	7	4.0	4.5	30	
	8	4.5	5.0	30	
Bering Sea bolide	1	0.1	5.0	50	3a–d
Mass movement on Redoubt volcano	1	0.5	8.0	50	4a–d
Bogoslof volcano	1	0.1	10.0	30	5a–d
Mount St. Helens and mass movement on Redoubt volcano	1	0.1	1.219	60	1f-k, 4f-k, 7
	2	1.219	2.338	58	
	3	2.338	3.456	56	
	4	3.456	4.575	54	
	5	4.575	5.694	52	
	6	5.694	6.813	50	
	7	6.813	7.931	48	
	8	7.931	9.050	46	
	9	9.050	10.169	44	
	10	10.169	11.288	42	
	11	11.288	12.406	40	
	12	12.406	13.525	38	
	13	13.525	14.644	36	
	14	14.644	15.763	34	
	15	15.763	16.881	32	
	16	16.881	18.0	30	
Bogoslof volcano, Bering Sea bolide and least trimmed squares	1	0.1	0.176	100	3f–k, 5f–k, and 6a–f,h–m
	2	0.176	0.308	90	
	3	0.308	0.541	80	
	4	0.541	0.949	70	
	5	0.949	1.665	60	
	6	1.665	2.922	50	

(Continued next page.)

TABLE 1 (continued)

Details for the Processing Parameters Used in the Examples, Including Band Number, Minimum and Maximum Frequency, Window Length, and Figure Number

Example	Band	Minimum Frequency (Hz)	Maximum Frequency (Hz)	Window Length (s)	Figure
	7	2.922	5.128	40	
	8	5.128	9.0	30	

0.1 and 10 Hz with a window length of 50 s with 50% overlap (Table 1). The narrow-band least-squares processing uses 16 bands linearly spaced between 0.1 and 18 Hz with an adaptive window length of 60–30 s with 50% overlap (Table 1).

Broad-band least-squares processing results including the filtered pressure trace between 0.5 and 10 Hz, MdCCM, back azimuth, and trace velocity from 01:00 to 02:30 UTC are shown by Figure 1a–e, respectively. Prior to the phreatic eruption onset at 01:26 UTC, the MdCCM values are low (Fig. 1b) with a scattered back azimuth (Fig. 1c), nonacoustic trace velocities (Fig. 1d), and high σ_{τ} values (Fig. 1e). At 01:26 UTC the MdCCM becomes elevated with realistic back azimuth for the volcano (153°) and trace velocity estimates until 01:41 UTC when the eruption signal briefly pauses. Although the MdCCM remains high for the remainder of the time period investigated, the back azimuth (Fig. 1c) transitions from Mount St. Helens (153°) to 285° \pm 10° at 01:58 UTC, indicating loss of dominance of this signal, which may falsely imply the end of the eruption, and subsequent dominance of the microbarom or surf.

The narrow-band least-squares processing results include the filtered pressure trace (Fig. 1g) from 0.5 to 10 Hz, MdCCM (Fig. 1h), back azimuth (Fig. 1i,l), trace velocity (Fig. 1j,m), and σ_{τ} (Fig. 1k) from 01:00 to 02:30 UTC. Results with MdCCM >0.6 are plotted in Figure 1i-m. Although the start time of the eruption is consistent with the broad-band leastsquares processing, the narrow-band least-squares processing does not show a pause in the eruption at 01:41 UTC but rather a cessation of higher frequencies (>5 Hz) for a few minutes while the lower frequencies continue to be coherent (Fig. 1h). The back azimuth (Fig. 1i,l) is directed toward Mount St. Helens for the entire eruption duration as well as a reasonable trace velocity (Fig. 1j,m). Toward the end of the eruption, the microbarom or surf begins to be detected in the lower frequency bands around 01:58 UTC (Fig. 11) with a more scattered back azimuth (Fig. 1i), but slightly higher frequencies from the eruption simultaneously continue to be detected for ~4 more minutes until 02:02 UTC. These simultaneous signals were not captured by broad-band least-squares processing because the highest signal-to-noise ratio source in the band dominates the detection. From this example, it is shown that the narrow-band least-squares processing can provide a more accurate representation of event duration than broad-band least squares, which loses coherence for part of the eruption

(~01:43–01:52 UTC), as well as interesting frequency changes throughout the eruption signal that would not be shown by broad-band least-squares processing.

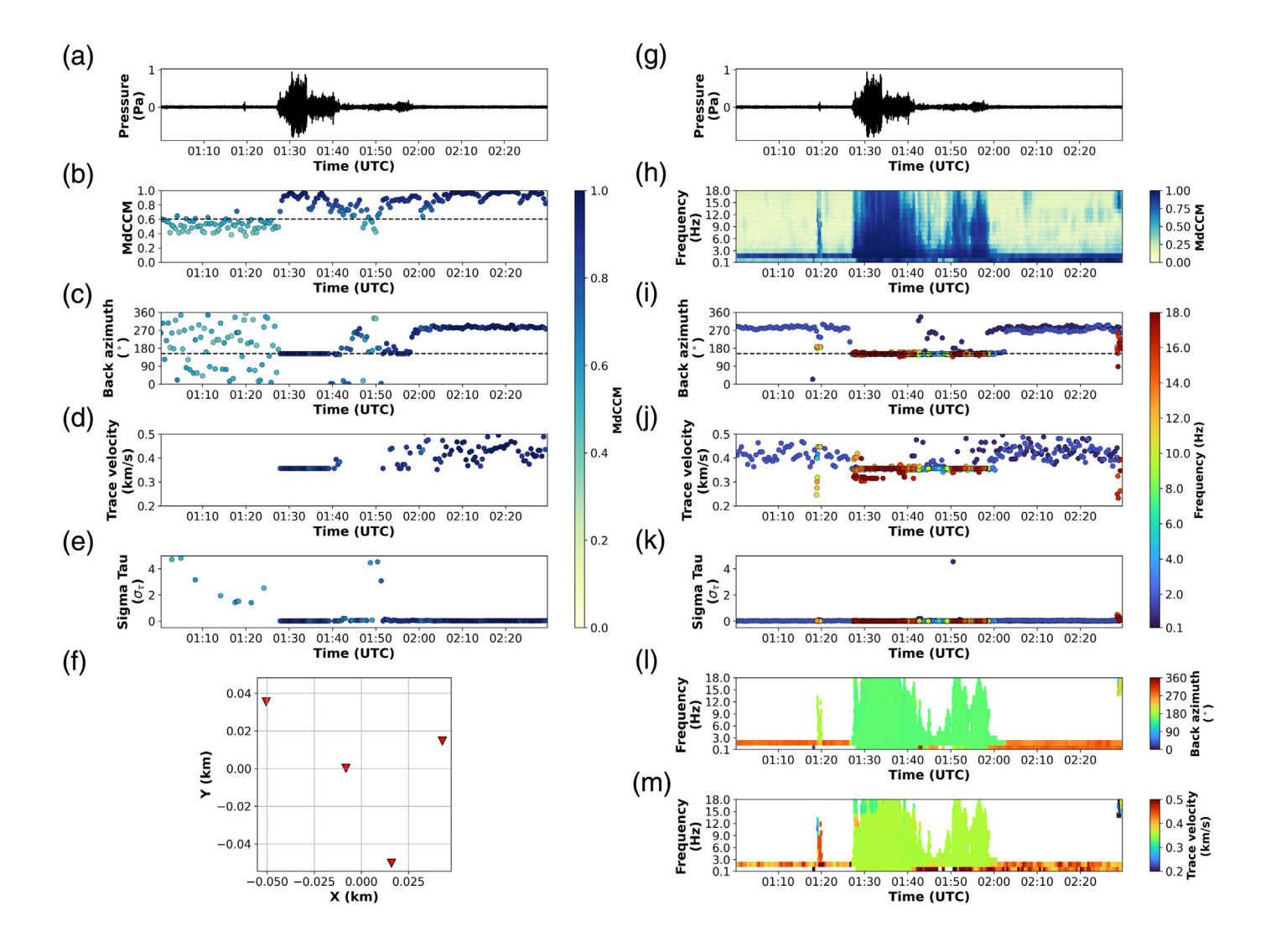
Multiweek trends

Using the CDWR array located near Mount St. Helens from the Eruption of Mount St. Helens, Washington section, we investigate a longer time period of 2.5 weeks from 01 to 16 November 2004. We use narrow-band least-squares processing parameters similar to the specifications that Matoza et al. (2007) used for PMCC processing in their figure 3. Our processing parameters here include eight frequency bands with linear spacing between 1 and 5 Hz, 30 s time windows with 50% overlap, and limiting the plotted results to those with MdCCM >0.55 and trace velocities between 0.25 and 0.45 km/s (Fig. 2). Similar to the findings of Matoza et al. (2007), we detect signals from multiple sources (Fig. 2). The ~2.5 Hz signals from the direction of Mount St. Helens (back azimuth of 153°) between 09 and 12 November are consistent with swarms of long period signals from the volcano (Matoza et al., 2007, 2009). Another continuous and coherent signal over most of the study period are the higher frequency detections (>3.5 Hz) from a back azimuth of ~200° (Portland, Oregon), as well as the towns north of it, suggesting the signals are cultural noise. In addition, lower frequency signals ~1 Hz have back azimiuths corresponding to the Pacific Ocean (~250°-350°). We find that narrow-band least-squares processing provides useful results for long-duration examples looking for trends over timescales of weeks to months.

Bering Sea bolide

On 19 December 2018, a bolide (meteor) that exploded over the Bering Sea was detected on the IMS station I53US in Fairbanks, Alaska (Arrowsmith *et al.*, 2021). I53US is an eight-element array with ~2 km aperture (Fig. 3f), sampling rate of 20 Hz, flat sensor response between 0.02 and 100 Hz, and a wind noise reduction system installed.

Least-squares array processing, both broad- and narrow-band, is applied to the I53US data from 01:45 to 02:05 UTC on 19 December 2018. Broad-band least-squares processing uses a bandpass filter between 0.1 and 5 Hz with a window length of 50 s with 50% overlap (Table 1). Narrow-band least-squares processing is implemented using eight bands with logarithmic



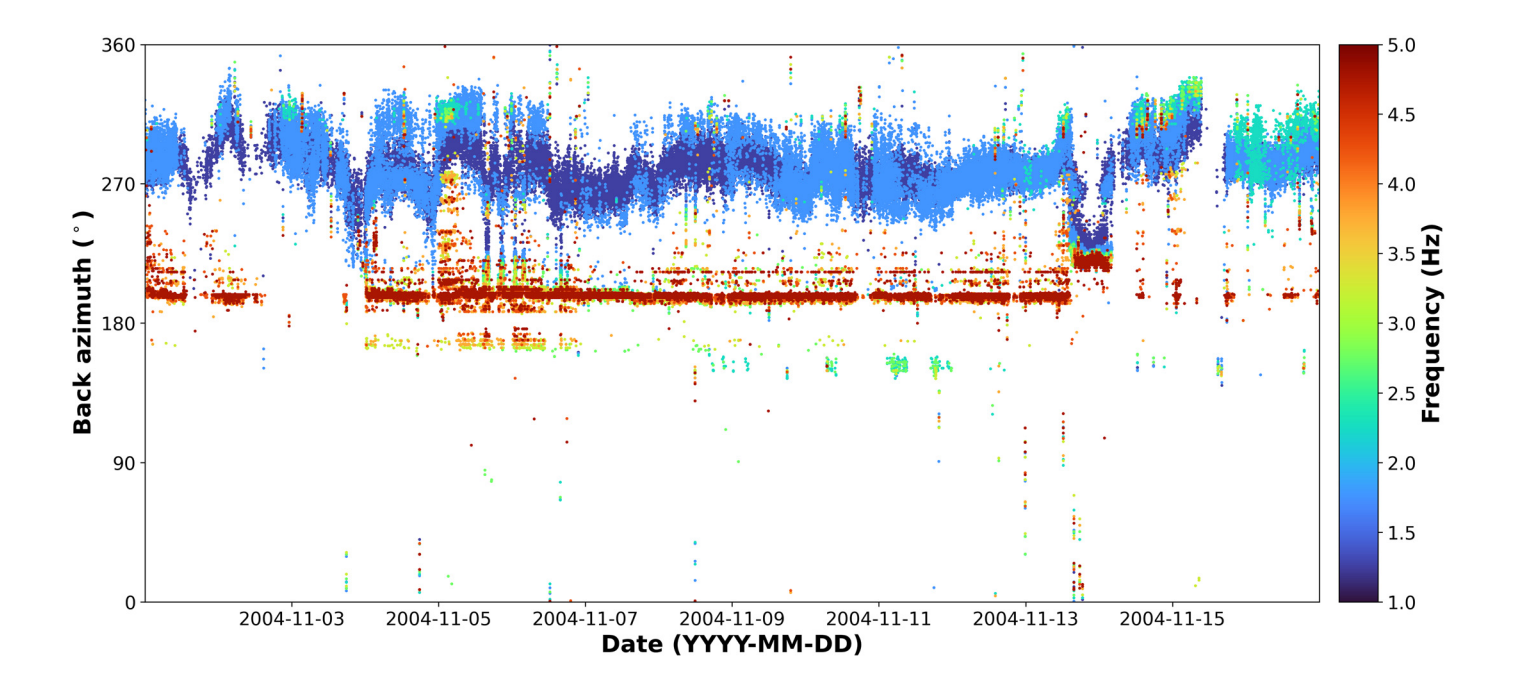
spacing between 0.1 and 9 Hz and an adaptive window length of 100 to 30 s with 50% overlap (Table 1).

Both the broad-band least-squares (Fig. 3a-e) and narrow-band least-squares processing (Fig. 3g-m) yield similar results. However, the narrow band processing allows for a more detailed investigation into the source, in which the signal starts off with lower frequencies, gradually includes higher frequencies, and then the frequency content more gradually decreases and tapers off during the rest of the signal (Fig. 3i,j,l,m). These changes in frequency content within the signal would not be apparent if broad-band least-squares processing was used and has implications for source (e.g., volcanic emissions, moving source, etc.) and propagation (e.g., atmospheric parameters, multipathing, etc.) characterization.

Surficial mass movement on Redoubt volcano, Alaska

Mass movement events can occur on steep slopes of volcanoes and be recorded using infrasound sensors at local and regional distances (e.g., Allstadt *et al.*, 2018; Toney *et al.*, 2021). They are typically characterized by their emergent

Figure 1. Array processing example from the 08 March 2005 Mount St. Helens eruption (09 March UTC, back azimuth 153°) using the Coldwater (CDWR) infrasound array data (Matoza et al., 2007). Broad-band least-squares array processing is shown on the left (a–e) with specifications of Type I Chebyshev bandpass filter between 0.1 and 10 Hz and window length of 50 s with 50% overlap and narrow-band least-squares implementation on the right (q-m) with specifications of 16 frequency bands with linear spacing between 0.1 and 18 Hz, an adaptive window length of 60 to 30 s with 50% overlap, and results with MdCCM >0.6 plotted in (i-m). Results from broad-band least-squares processing are (a) pressure trace from element one (filtered between 0.5 Hz and the maximum frequency from broad-band least-squares processing), (b) median cross-correlation maxima, (c) back azimuth (true back azimuth denoted by dotted horizontal line), (d) trace velocity, and (e) sigma tau (σ_{τ}) . Array geometry is shown in panel (f). Results from narrow-band least-squares processing are (g) pressure trace from element one (same as panel a), (h) median cross-correlation maxima, (i,l) back azimuth (true back azimuth in panels (c,i) denoted by dotted horizontal line), (j,m) trace velocity, and (k) sigma tau (σ_{τ}). The color version of this figure is available only in the electronic edition.



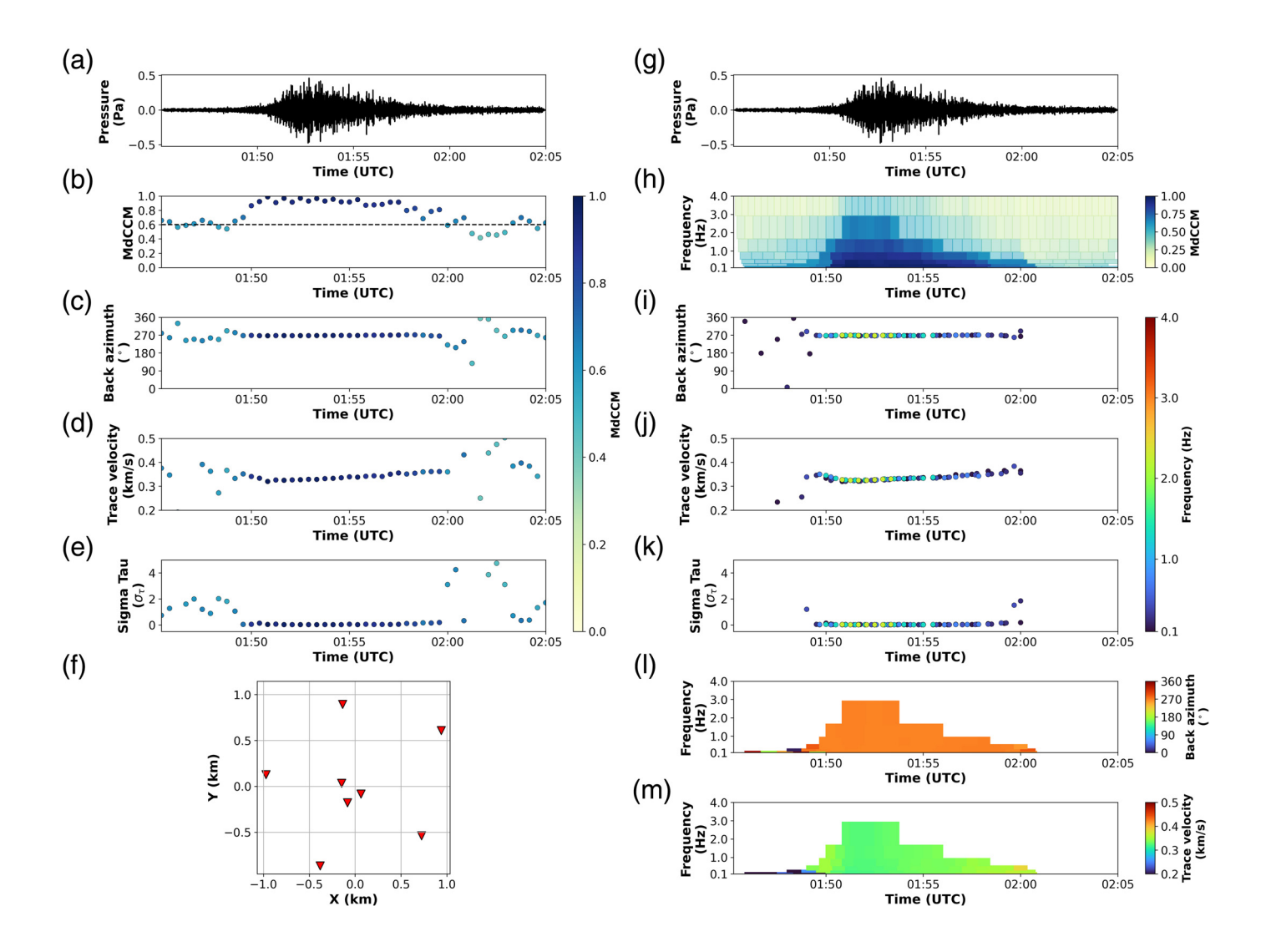
signal onset and extended duration (as compared to a simple explosion signal), which can make the distinction between these signals and wind noise challenging (Allstadt *et al.*, 2018). A mass movement on Redoubt volcano was detected on the local seismic network on 3 November 2021, but no infrasound signal was clear in the broad-band Alaska Volcano Observatory (AVO) infrasound processing for the nearby AVO KENI array. The KENI array is located 93 km from Redoubt volcano, Alaska (back azimuth of 260°), and includes six Chaparral 64-Vx sensors with a flat response of 0.03–245 Hz sampled at 100 Hz spread over ~170 m (Fig. 4f) and wind noise reduction domes installed.

We apply broad- and narrow-band least-squares processing to the data from 15:30 to 15:50 UTC on 03 November 2021. Processing parameters for the broad-band least-squares analysis include data bandpass filtered between 0.5 and 8 Hz (consistent with AVO's real-time monitoring frequency limits) with a window length of 50 s with 50% overlap (Table 1). Narrow-band least-squares processing includes 16 bands with linear spacing between 0.1 and 18 Hz and an adaptive window length of 60–30 s with 50% overlap (Table 1).

The mass movement signal is not observed in broad-band least-squares processing (Fig. 4a-e), likely due to the microbarom and surf dominating the signal causing high MdCCM (Fig. 4b) and high-frequency content of the low amplitude mass movement signal that is above the band of typical processing (>10 Hz). We also note that the trace velocity estimates for the ordinary least-squares processing in this broad frequency band were not within the expected range for acoustic signals (0.2–0.5 km/s, Fig. 4d). Applying narrow-band least-squares processing allows for the "clutter" sources and mass movement signal to be separated due to processing occurring in distinct frequency bands, thus allowing

Figure 2. Array processing multiweek example using the CDWR array near Mount St. Helens from 01 to 16 November 2004 (compare with fig. 3 of Matoza et al., 2007). Parameters for narrow-band least-squares processing include eight frequency bands with linear spacing between 1 and 5 Hz, 30 s time windows with 50% overlap, and results with median cross-correlation maxima (MdCCM) >0.55 that also have trace velocities between 0.25 and 0.45 km/s plotted. The ~2.5 Hz signals from the direction of Mount St. Helens (back azimuth of 153°) between 09 and 12 November are consistent with swarms of long period (LPs) signals from the volcano (Matoza et al., 2007, 2009). The higher frequency detections (>3.5 Hz) are likely cultural noise from a back azimuth of ~200° (Portland, Oregon), as well as the towns north of Portland. The lower frequency signals ~1 Hz have back azimuths corresponding to the Pacific Ocean (~250°-350°). The color version of this figure is available only in the electronic edition.

for multiple simultaneous sources to be observed (seen clearly in Fig. 41). The mass movement signal lasting roughly 5 min is clearly visible with a high MdCCM between 7 and 13 Hz (Fig. 4h) and back azimuth consistent with Redoubt volcano (Fig. 4i). Two other distinct sources are also clearly visible for the entire duration of the data analyzed. The lowest frequency band (<1 Hz) is interpreted to be the microbarom signal due to its low frequency (Fig. 4h) and scatter in back azimuth 180° ± 10° (Fig. 4i). In the second to the lowest frequency band (~1-2 Hz), another persistent source is detected and interpreted to be surf with frequencies just above the microbarom (e.g., Le Pichon et al., 2004) and a back azimuth roughly the same as Redoubt (260°, Fig. 4i). This example highlights the capabilities of narrow-band least-squares processing for distinguishing between multiple simultaneous sources with distinct frequency content, allowing for enhanced detection of



the sources of interest that may be otherwise obscured. In addition, narrow-band least-squares processing can be performed for a wider range of frequencies, allowing for low amplitude, higher frequency signals such as a mass movement to be detected even while a low frequency signal such as the microbarom or surf dominates typical frequencies analyzed.

Eruption of Bogoslof volcano, Alaska

The 2016–2017 eruption of Bogoslof volcano, Alaska, United States had at least 70 explosive episodes over 9 months that were often recorded on six infrasound arrays operated by AVO (Lyons et al., 2020). Event 14 (02 January 2017 at 22:56 UTC, Coombs et al., 2018) was not detected by the Dillingham Infrasound Array (DLL) with the parameters of Lyons et al. (2020) used to make the catalog of explosive events detected using infrasound. However, atmospheric reconstruction and propagation modeling by Schwaiger et al. (2020) suggests that a detection would be predicted at the time of the eruption for this array. DLL is a regional array operated by AVO located 816 km from Bogoslof (back azimuth of 229°). The array is ~1 km in aperture (Iezzi et al., 2019; Lyons et al., 2020) and

Figure 3. Array processing example from the 19 December 2018 Bering Sea bolide using the I53US infrasound array data. Broad-band least-squares array processing is shown on the left (a–e) with specifications of Type I Chebyshev bandpass filter between 0.1 and 5 Hz and window length of 50 s with 50% overlap and narrow-band least-squares implementation on the right (g–m) with specifications of eight frequency bands with logarithmic spacing between 0.1 and 9 Hz, an adaptive window length of 100–30 s with 50% overlap, and results with MdCCM >0.6 plotted in (i–m). Note: The frequency axes are zoomed to better depict the low frequency results. Array geometry is shown in panel (f). Subplots are the same as Figure 1. The color version of this figure is available only in the electronic edition.

at the time consisted of six Chaparral Physics Model 50a sensors (five elements working during this explosive episode, Fig. 5f) with a flat response from 0.02 to 50 Hz and a wind noise reduction system installed (Lyons *et al.*, 2020).

Least-squares array processing, both broad- and narrow-band, is applied to the DLL data for event 14. Broad-band least-squares processing uses data bandpass filtered between 0.1 and 10 Hz and a window length of 30 s with 50% overlap

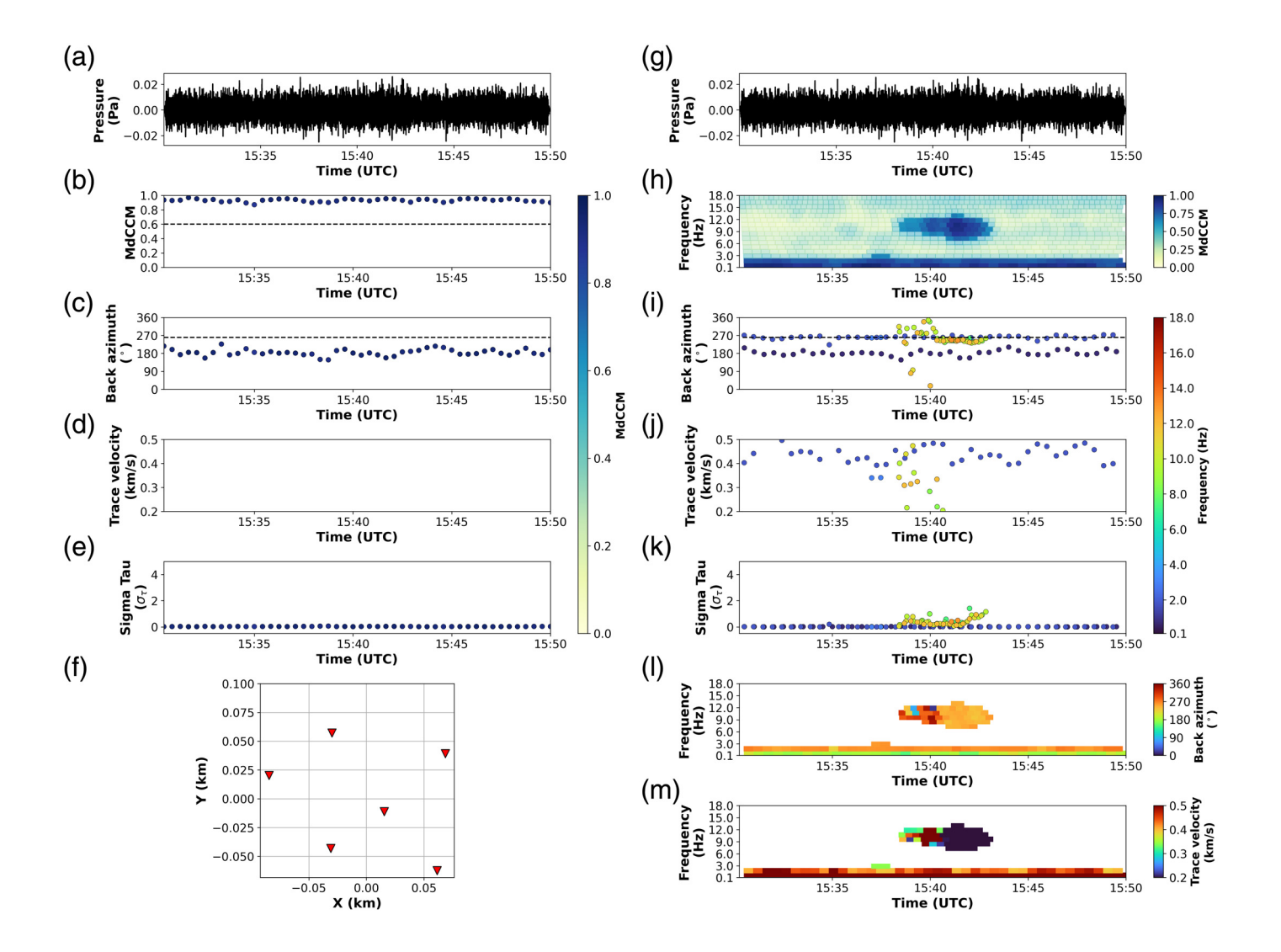


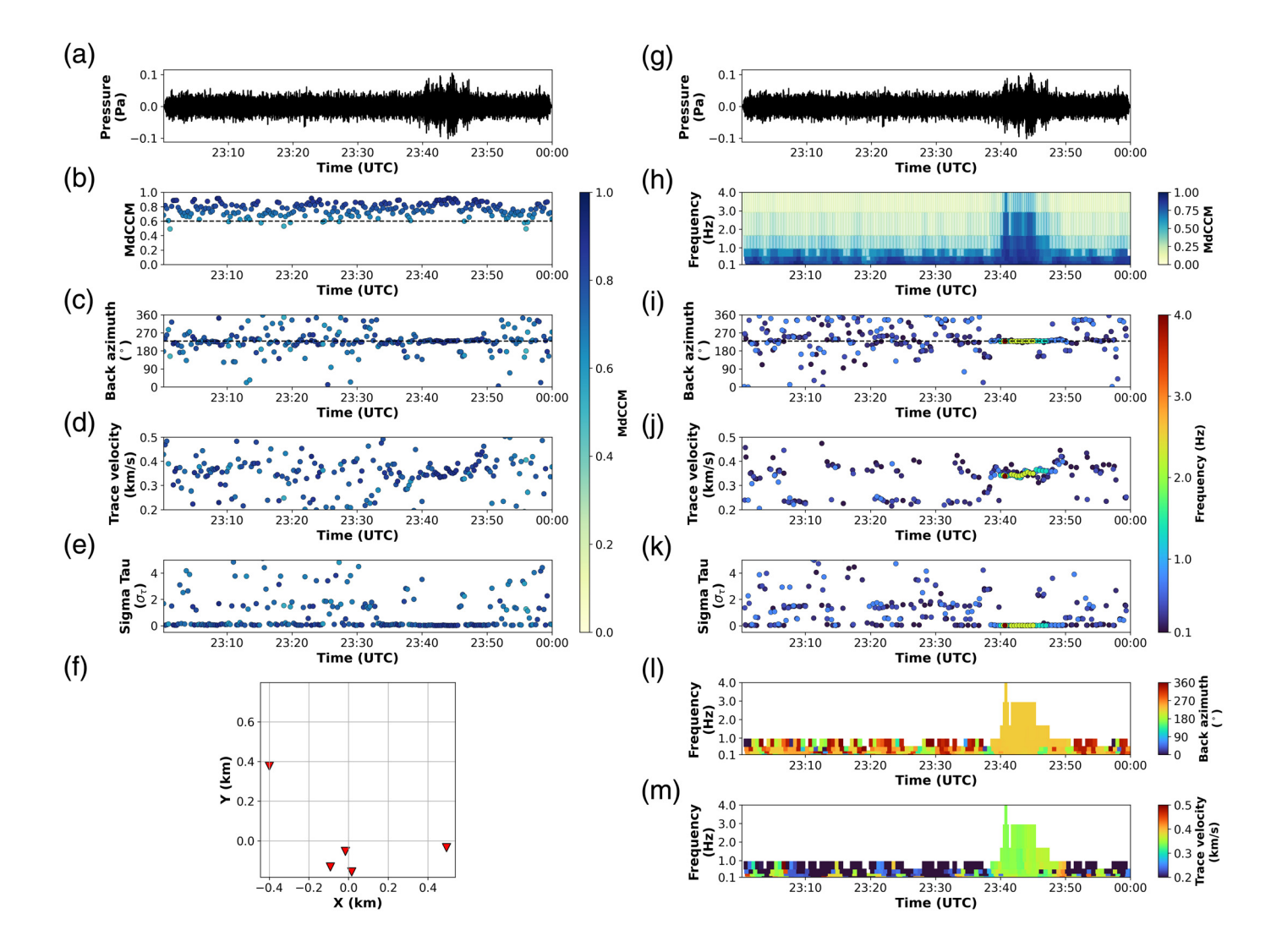
(Table 1), which is similar to those used by Lyons *et al.* (2020) to make the catalog of Bogoslof events detected using AVO's regional infrasound arrays. Narrow band processing uses eight bands with logarithmic spacing between 0.1 and 9 Hz, and an adaptive window length of 100 to 30 s with 50% overlap (Table 1).

Broad-band least-squares processing results are shown in Figure 5a-e, in which no clear eruption signal can be seen due to elevated noise and, therefore, high MdCCM at the array that obscures the eruption signal. However, with narrowband least-squares processing (Fig. 5g-m), the eruption signal is evident below 3 Hz from 23:38 to 23:48 UTC (origin time of 22:58 UTC given an average ~41 minutes travel time to the array, Lyons et al., 2020). This signal is clearly shown by high values of MdCCM (Fig. 5h), back azimuth consistent with Bogoslof (Fig. 5i), and reasonable trace velocities (Fig. 5j,m). This example shows that our narrow-band least-squares array processing method may increase the ability to detect eruption signals that may not be detected using broad-band least-squares processing, therefore improving eruption monitoring capabilities.

Figure 4. Array processing example from the 03 November 2021 mass movement on Redoubt volcano, Alaska (back azimuth 260°) using the KENI infrasound array data. The mass movement was detected on the local seismic network, but no infrasound signal was clear in the broad band Alaska Volcano Observatory (AVO) infrasound processing for the KENI array. Broad-band least-squares array processing is shown on the left (a-e) with specifications of Type I Chebyshev bandpass filter between 0.5 and 8 Hz and window length of 50 s with 50% overlap and narrow-band least-squares implementation on the right (g-m) with specifications of 16 frequency bands with linear spacing between 0.1 and 18 Hz, an adaptive window length of 60 to 30 s with 50% overlap, and results with MdCCM >0.6 plotted in (i-m). Array geometry is shown in panel (f). Subplots are the same as Figure 1. The color version of this figure is available only in the electronic edition.

LTS implementation

We investigate another explosive event from Bogoslof volcano to highlight the utility of the LTS algorithm of Bishop *et al.* (2020). Event 48 (10 June 2017, Coombs *et al.*, 2018) was not detected at the Adak infrasound array (ADKI) in real time, because one of the elements (element 2) of the array had a



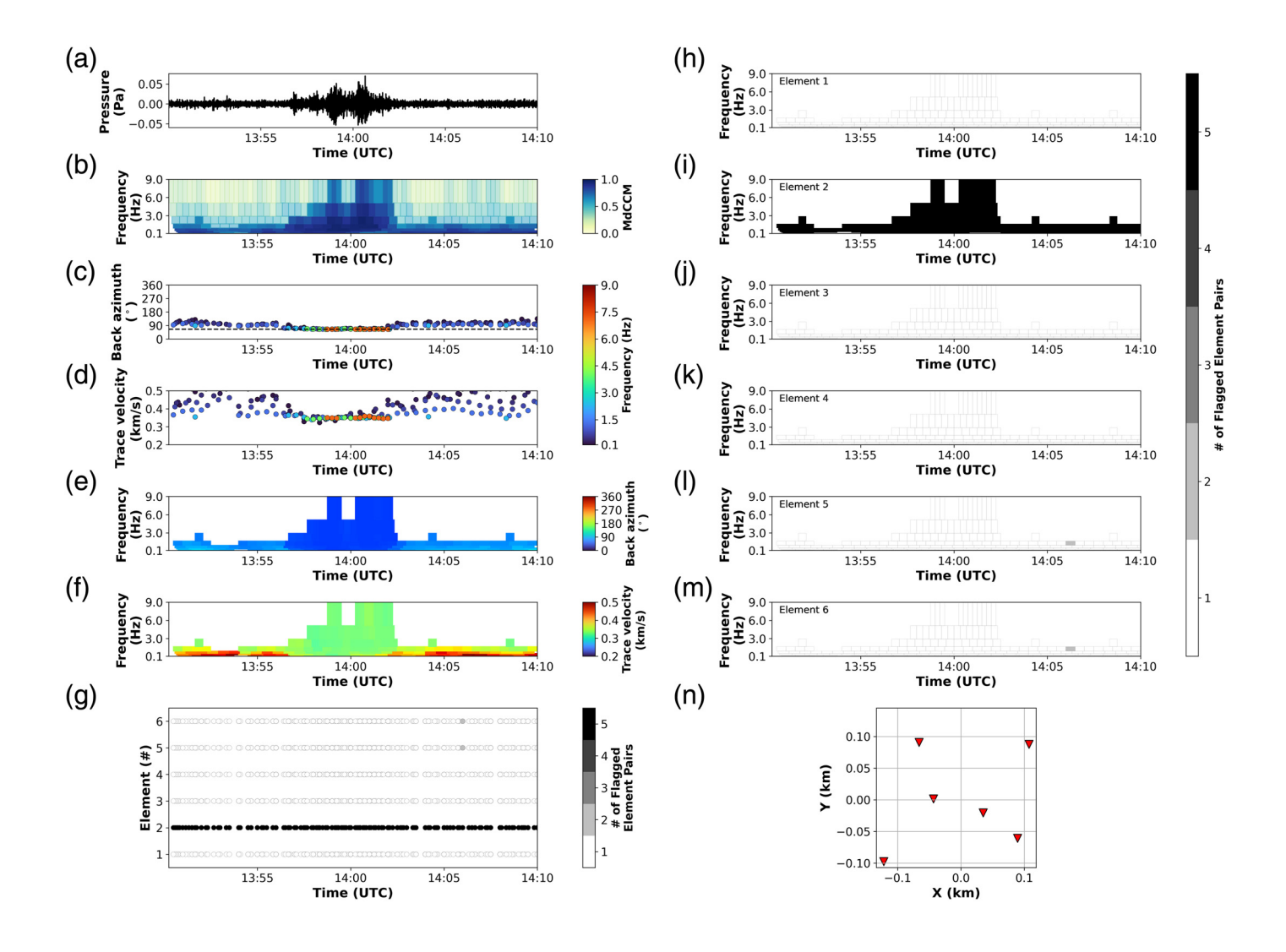
reversed polarity (that was unknown in real time). Bishop *et al.* (2020) investigated this example, finding that the application LTS instead of least-squares shows that element 2 was consistently dropped from the array processing algorithm. ADKI is located 621 km from Bogoslof with an aperture of ~200 m (Fig. 6n), consisted of six Chaparral Model 25Vx sensors sampled at 100 Hz, and 1.2 m diameter aluminum mesh wind noise reduction domes (Lyons *et al.*, 2020).

Narrow-band LTS processing is applied to the ADKI data using ALPHA = 0.5 with eight frequency bands with logarithmic spacing between 0.1 and 9 Hz, and an adaptive window length of 100-30 s with 50% overlap (Table 1).

Results from narrow band processing are shown in Figure 6a–f, in which the eruption signal can clearly be seen from 13:56:30 to 14:02 UTC with high MdCCM (Fig. 6b), back azimuth consistent with Bogoslof (65°, Fig. 6c,e), and reasonable trace velocities (Fig. 6d,f). Microbarom and surf are detected before and after the eruption signal with high MdCCM values (Fig. 6b) and low frequency content (Fig. 6b–f) from a similar back azimuth to Bogoslof. An overview of dropped elements from the LTS implementation is shown by Figure 6g, with

Figure 5. Array processing example from the 02 January 2017 eruption of Bogoslof volcano, Alaska (event 14 in Lyons et al., 2020, back azimuth 229°) using the Dillingham Infrasound Array (DLL) infrasound array data. The event was not included in the catalog of explosive events detected at this array by Lyons et al. (2020). Broad-band least-squares array processing is shown on the left (a-e) with specifications of Type I Chebyshev bandpass filter between 0.1 and 10 Hz and window length of 30 s with 50% overlap and narrow-band least-squares implementation on the right (q-m) with specifications of eight frequency bands with logarithmic spacing between 0.1 and 9 Hz, an adaptive window length of 100–30 s with 50% overlap, and results with MdCCM >0.6 plotted in (i-m). Note: The frequency axes are zoomed to better depict the low frequency results. Array geometry is shown in panel (f). Subplots are the same as Figure 1. The color version of this figure is available only in the electronic edition.

detailed results of the dropped stations for the narrow frequency bands shown in Figure 6h-m for elements 1-6, respectively. Element 2 is consistently dropped from analysis (similar to Bishop *et al.*, 2020). This example shows that LTS can provide robust array processing results and insight into array



performance (e.g., timing errors and sensor issues), even when applied in narrow bands. The implementation of LTS in narrow bands also allows for LTS to determine problematic sensors without having to "fine-tune" of frequency limits based on individual array and signal characteristics.

Processing Parameter Investigation and Discussion

In this study, we present a narrow-band least-squares array processing algorithm and associated open-source code, which allows for a more detailed time–frequency signal characterization over broad-band least-squares infrasound array processing. Our algorithm can incorporate a measure of the variance of the time delays between array elements (σ_{τ}) as well as LTS (Bishop *et al.*, 2020) for improved processing capabilities. Although there is an increase in the number of user defined parameters for narrow-band least-squares over broad-band least-squares, we note that the parameters may largely be consistent and should not require many changes between examples thus making it more user friendly. For example, broad-band least-squares implementation requires a choice of the single

Figure 6. Array processing example from the 10 June 2017 eruption of Bogoslof volcano. Alaska (back azimuth 65°) using the Adak infrasound array (ADKI) infrasound array data. Narrowband least-squares implementation using least trimmed squares (LTS) with ALPHA = 0.5 on the left (a–f) with specifications of eight frequency bands with logarithmic spacing between 0.1 and 9 Hz, and an adaptive window length of 100 to 30 s with 50% overlap. Results from narrow-band least-squares processing are (a) pressure trace from element one (filtered between 0.5 and 9 Hz), (b) median cross-correlation maxima, (c,e) back azimuth, and (d,f) trace velocity. An overview of dropped elements from the LTS implementation is shown in (g), while detailed results of the dropped stations for frequency bands are shown in (h-m) for elements 1-6, respectively. Results with MdCCM >0.6 plotted in panels (c-m). Array geometry is shown in panel (n). The color version of this figure is available only in the electronic edition.

frequency band limits, which often requires a tradeoff between limiting clutter signals while trying to retain the anticipated signals of interest. In the case of the mass movement at Redoubt, the signal of interest was 7–13 Hz, which is above the normal frequency limits used for explosion monitoring, and thus the

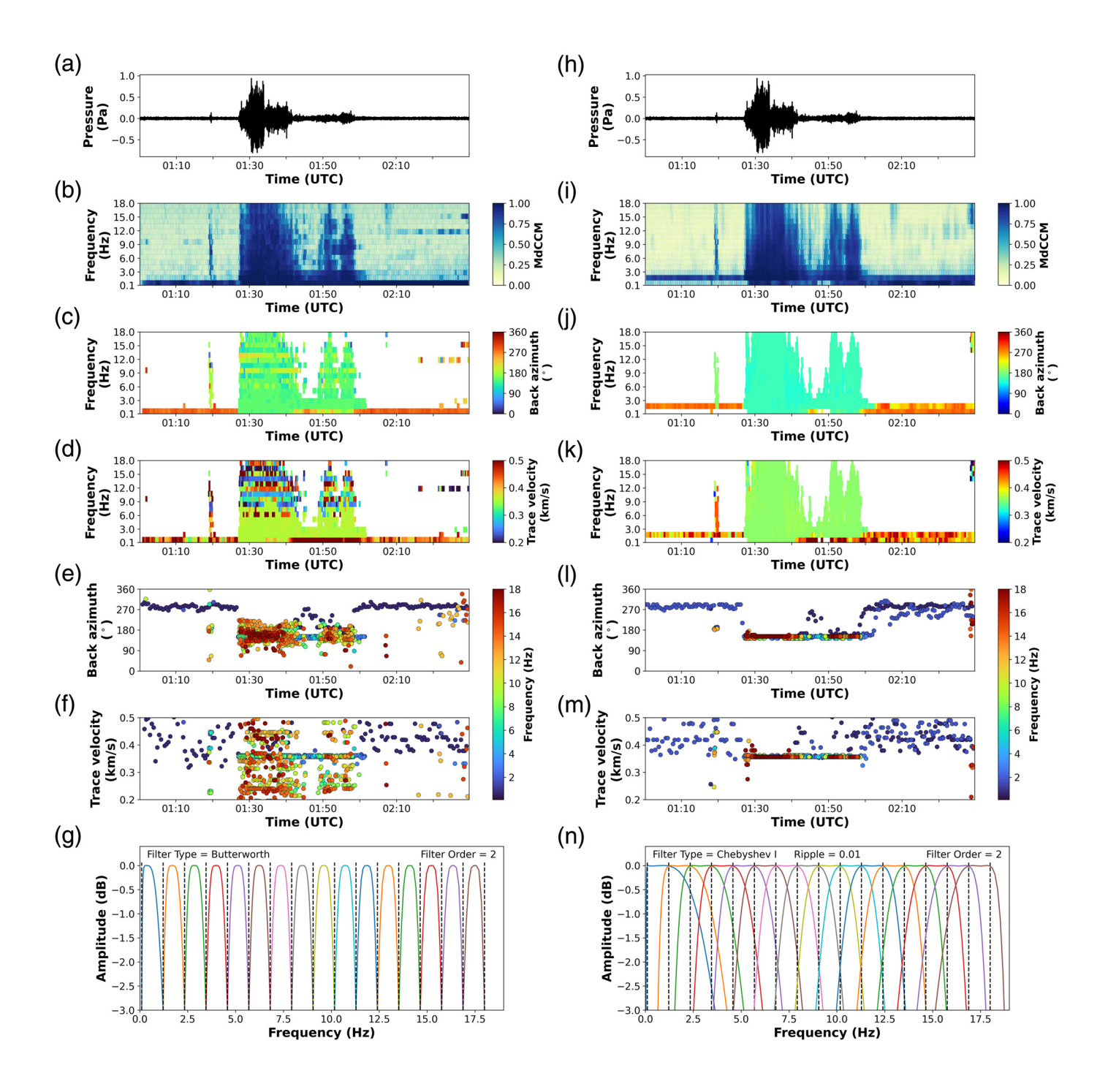
signal was not captured by AVO's typical processing. With narrow-band least-squares, we show that the same upper and lower frequency limits can be used for a variety of sources from explosions at local scales to mass movements at regional distances to bolides at remote distances. Examples of previously "hidden" signals, such as the Bogoslof explosive event (Fig. 5) and the mass movement on Redoubt volcano (Fig. 4), visually show increased detection capability using our narrow-band least-squares algorithm over broad-band least squares. For simplicity, we use a MdCCM threshold (e.g., 0.6), back azimuth close to true, and reasonable trace velocity estimates (e.g., 0.2-0.5 km/s) as a way to consider whether or not an event was detected. Future work could include more complex detection algorithms that combine multiple detections from individual time-frequency cells (e.g., PMCC groups sets of timefrequency band pair "pixels" into "families", Cansi, 1995; Cansi and Klinger, 1997). This may improve monitoring capabilities such as those at a volcano observatory, while considering the increased potential for "false alarms" due to increased number of frequency bands. We suggest that another way to mitigate false detections in an operational setting is to use the broad band processing for detection and the narrow band processing for near real-time manual analyst review.

We investigate two common filter types for the narrow band processing results by revisiting the 08 March 2005 eruption of Mount St. Helens CDWR array data. A Butterworth filter has a less steep roll-off but is flat in the passband with results shown in Figure 7a-g. Another common filter type is the Type I Chebyshev filter, which generally has a steeper roll-off but ripples in the passband (Fig. 7h-n, note there is a tradeoff between ripple parameter and steepness of roll-off). For the Type I Chebyshev filter, we note that increasing the ripple leads to a steeper roll-off, and our low ripple value of 0.01 results in a less steep roll-off than the Butterworth filter. MdCCM results using the Chebyshev filter (Fig. 7i) show a greater contrast between signal and background noise than the Butterworth filter (Fig. 7b), as shown by the lower MdCCM values (deeper blue colors in Fig. 7i) surrounding the coherent signal than in Fig. 7b. Results using Chebyshev filters (Fig. 7h-n) show less scatter in the trace velocity and back azimuth results than those using Butterworth filters (Fig. 7a-g). This may be due to Butterworth filters causing the narrow bands to be even narrower than specified (Fig. 7g), whereas the Type I Chebyshev filter has more overlap between the narrow bands (Fig. 7n). Although not shown, we note that there was no notable difference between the two filter types for the standard leastsquares processing due to the single broad frequency bandpass filter. Overall, the results using Chebyshev filters (Fig. 7h-n) seems to yield cleaner results than those using Butterworth filters (Fig. 7a-g) for the narrow-band least-squares processing. Therefore, the results suggest using Type I Chebyshev filtering for narrow-band least-squares processing (similar to that of PMCC, e.g., Arrowsmith and Hedlin, 2005; Matoza et al., 2013).

Although the narrow band implementation of the leastsquares array processing algorithm provides improved processing capabilities, limitations of the narrow frequency band width should be considered. Processing over narrow frequency bands affects both signal detection and parameter estimation, which is the focus of this article. If the frequency band widths (B) are too narrow or the window lengths (T) are too short, spurious correlations can occur. We quantify this trade off with the time-bandwidth product (BT). Although a detailed analysis of the effect of varying BT on our detections is beyond the scope of this article, we note that in the presence of a correlated signal the F-statistic (e.g., Shumway, 1971; Smart and Flinn, 1971) is distributed according to a noncentral F-distribution with degrees of freedom that are functions of BT (Shumway et al., 1999; Arrowsmith et al., 2009). In this work, the peak value of our cross correlations as well as the uncertainty in the location of the cross-correlation peak value also depend on BT (Bendat and Piersol, 2000). For our least-squares parameter estimates, this variability due to small BT could affect our estimates of the optimal slowness vector. Following Bendat and Piersol (2000), we suggest that BT >5 to minimize spurious correlations. This would partially be dependent on the filter type, as the flat passband for a Butterworth filter is narrower than the flat passband for a Type I Chebyshev filter (Fig. 7g,n). We note that array response is dependent on the array aperture (Gibbons et al., 2008; Ruigrok et al., 2017) and generally improves with band width. This is an important consideration for narrow band processing, because not all array configurations are suitable for every narrow frequency band used in analysis and can limit the accuracy for narrow band processing. Future work may include synthetic testing to evaluate these effects on the specific deployment scenarios but is beyond the scope of this work.

Conclusions

We present a new open-source multiple sequential narrow-band least-squares processing tool for infrasound array data. The algorithm provides an improvement in detection capabilities over broad-band least-squares array processing by allowing a more detailed time-frequency signal characterization. This capability can be utilized in near real-time volcano monitoring to identify signals that may be otherwise undetected. Improvements of the multiple narrow band processing over broad-band least squares include: (1) improved ability to distinguish between multiple sources with different frequency content such as the microbarom and/or surf from signals of interest, (2) more accurate representation of event duration, (3) enhanced signal detection capabilities, (4) improved ability to illuminate changes in frequency content within a signal, (5) upgraded capability to distinguish between multiple simultaneous sources if distinct in their frequency content, and (6) does not require "fine tuning" of frequency limits based on individual array and signal characteristics. We incorporate the calculation of sigma tau (σ_{τ}) as a measure of planarity of the wavefield across the array as well as



the ability to incorporate the LTS algorithm of Bishop *et al.* (2020) to improve signal processing and insight into array performance. Our examples include short duration (e.g., minutes to hours) as well as longer duration (e.g., weeks), showing useful array processing results over a variety of timescales. We find that the Type I Chebyshev filter appears to provide better results than a Butterworth filter for the multiple narrow band implementation of the least-squares algorithm. Because the narrow-band least-squares implementation has been parallelized, the computation time can be similar to broad-band least-squares when the number of bands is less than the number of cores, making this implementation feasible for real-time monitoring situations.

Figure 7. (a–g) Comparison between Butterworth and (h–n) Type I Chebyshev filters for narrow band processing using the 08 March 2005 Mount St. Helens eruption (09 March UTC, back azimuth 153°) using the CDWR infrasound array data. Specifications of 16 frequency bands with linear spacing between 0.1 and 18 Hz, an adaptive window length of 60 to 30 s with 50% overlap, and results with MdCCM >0.6 plotted in panels (c–f, j–m). (a,h) Pressure trace from element one filtered between 0.5 and 18 Hz, (b,i) median cross-correlation maxima, (c,j) back azimuth, (d,k) trace velocity, (e,i) back azimuth scatter plot, (f,m) trace velocity scatter plot, and (g,n) amplitude of narrow filter bands. This example shows that type I Chebyshev filters appears to provide better results than Butterworth filters for narrow-band least-squares processing. The color version of this figure is available only in the electronic edition.

Data and Resources

The narrow-band least-squares code repository is publicly accessible on Github (https://github.com/amiezzi/narrow_band_least_squares, last accessed April 2022) and relies upon another publicly accessible repository on Github (https://github.com/uafgeotools/array_processing, last accessed February 2022). Most datasets used in the examples are accessible on Incorporated Research Institutions for Seismology (IRIS) under network codes AV (DLL, KENI) and IM (I53US). The data from the Mount St. Helens eruption (Coldwater [CDWR]) are available through Natural Resources Canada (NRCan)/CHIS autodrm tools (https://earthquakescanada.nrcan.gc.ca/stndon/AutoDRM/index-en.php, last accessed May 2022) using the DC network code and station names MSH21, MSH22, MSH23, and MSH24, as well as in a Dryad Data Repository (Matoza and Iezzi, 2022, https://doi.org/10.25349/D92W38) (please also cite Matoza et al. (2007) for usage of this data).

Declaration of Competing Interests

The authors acknowledge that there are no conflicts of interest recorded.

Acknowledgments

The authors would like to thank Steven Gibbons and an anonymous reviewer, as well as editor Allison Bent for their comments on the manuscript. The authors would also like to thank Oliver Lamb and John Lyons for their feedback and testing the code prior to public release. The authors acknowledge support from National Science Foundation (NSF) Grant Numbers EAR-1952392 (Alexandra M. Iezzi) and EAR-1847736 (Robin S. Matoza). This work was supported by the Nuclear Arms Control Technology (NACT) program at the Defense Threat Reduction Agency (DTRA) through Contract Number HDTRA121C0030. Cleared for release.

References

- Allstadt, K. E., R. S. Matoza, A. B. Lockhart, S. C. Moran, J. Caplan-Auerbach, M. M. Haney, W. A. Thelen, and S. D. Malone (2018). Seismic and acoustic signatures of surficial mass movements at volcanoes, *J. Volcanol. Geotherm. Res.* 364, 76–106.
- Arrowsmith, S. J., and M. A. Hedlin (2005). Observations of infrasound from surf in southern California, *Geophys. Res. Lett.* **32**, no. 9, 1–4.
- Arrowsmith, S., P. Negraru, and G. Johnson (2021). Bolide energetics and infrasound propagation: Exploring the 18 December 2018 Bering Sea event to identify limitations of empirical and numerical models, *Seismic Record* 1, no. 3, 164–171.
- Arrowsmith, S. J., R. Whitaker, C. Katz, and C. Hayward (2009). The F-detector revisited: An improved strategy for signal detection at seismic and infrasound arrays, *Bull. Seismol. Soc. Am.* **99**, no. 1, 449–453
- Bendat, J., and A. Piersol (2000). Random Data: Analysis and Measurement Procedures, John Wiley & Sons, Inc, New York.
- Bishop, J. W., D. Fee, and C. A. L. Szuberla (2020). Improved infrasound array processing with robust estimators, *Geophys. J. Int.* **221**, no. 3, 2058–2074.
- Blandford, R. R. (1974). An automatic event detector at the Tonto forest seismic observatory, *Geophysics* **39**, no. 5, 633–643.
- Brachet, N., D. Brown, R. Le Bras, P. Mialle, and J. Coyne (2010). Monitoring the earth's atmosphere with the Global IMS

- Infrasound Network, in *Infrasound Monitoring for Atmospheric Studies*, A. Le Pichon, E. Blanc, and A. Hauchecorne (Editors), Springer, Dordrecht, The Netherlands.
- Cansi, Y. (1995). An automatic seismic event processing for detection and location: The P.M.C.C. method, *Geophys. Res. Lett.* **22**, no. 9, 1021–1024.
- Cansi, Y., and Y. Klinger (1997). An automated data processing method for mini-arrays, CSEM/EMSC European-Mediterranean Seismological Centre Newsletter, Vol. 11, 1021–1024.
- Christie, D. R., and P. Campus (2010). The IMS infrasound network: Design and establishment of infrasound stations, in *Infrasound Monitoring for Atmospheric Studies*, A. Le Pichon, E. Blanc, and E. Hauchecorne (Editors), Springer, Dordrecht, The Netherlands, 29–75.
- Coombs, M. L., A. G. Wech, M. M. Haney, J. J. Lyons, D. J. Schneider, H. F. Schwaiger, K. L. Wallace, D. Fee, J. T. Freymueller, J. R. Schaefer, et al. (2018). Short-term forecasting and detection of explosions during the 2016–2017 eruption of Bogoslof volcano, Alaska, Front. Earth Sci. 6, 1–17.
- De Angelis, S., D. Fee, M. Haney, and D. Schneider (2012). Detecting hidden volcanic explosions from Mt. Cleveland volcano, Alaska with infrasound and ground-coupled airwaves, *Geophys. Res. Lett.* **39**, no. 21, doi: 10.1029/2012GL053635.
- De Angelis, S., M. M. Haney, J. J. Lyons, A. Wech, D. Fee, A. Diaz-Moreno, and L. Zuccarello (2020). Uncertainty in detection of volcanic activity using infrasound arrays: Examples from Mt. Etna, Italy, *Front. Earth Sci.* **8**, 1–11.
- Fee, D., and R. S. Matoza (2013). An overview of volcano infrasound: From Hawaiian to Plinian, local to global, *J. Volcanol. Geotherm. Res.* **249**, 123–139.
- Fee, D., R. Waxler, J. Assink, Y. Gitterman, J. Given, J. Coyne, P. Mialle, M. Garces, D. Drob, D. Kleinert, et al. (2013). Overview of the 2009 and 2011 Sayarim infrasound calibration experiments, J. Geophys. Res. 118, no. 12, 6122–6143.
- Gabrielson, T. (2017). State-of-health assessment of infrasound elements using operational data, *Infrasound Technology Workshop* 2017 Book of Abstracts.
- Garces, M. A. (2013). On infrasound standards, part 1: Time, frequency, and energy scaling, *InfraMatics* 2, no. 2, 13–35.
- Gibbons, S., F. Ringdal, and T. Kvaerna (2008). Detection and characterization of seismic phases using continuous spectral estimation on incoherent and partially coherent arrays. *Geophys. J. Int.* **172**, 405–421.
- Green, D. N., and D. Bowers (2010). Estimating the detection capability of the International Monitoring System infrasound network, *J. Geophys. Res.* **115**, no. 18, 1–18.
- Haney, M., A. Van Eaton, J. Lyons, R. Kramer, D. Fee, and A. Iezzi (2018). Volcanic thunder from explosive eruptions at Bogoslof volcano, Alaska, *Geophys. Res. Lett.* 45, no. 8, 3429–3435.
- Hedlin, M. A. H., B. Alcoverro, and G. D'Spain (2003). Evaluation of rosette infrasonic noise-reducing spatial filters, *J. Acoust. Soc. Am.* 114, no. 4, 1807–1820.
- Iezzi, A. M., H. F. Schwaiger, D. Fee, and M. M. Haney (2019). Application of an updated atmospheric model to explore volcano infrasound propagation and detection in Alaska, *J. Volcanol. Geotherm. Res.* 371, 192–205.

- Landès, M., L. Ceranna, A. Le Pichon, and R. S. Matoza (2012). Localization of microbarom sources using the IMS infrasound network, J. Geophys. Res. 117, no. 6, 1–6.
- Le Pichon, A., L. Ceranna, M. Garcés, D. Drob, and C. Millet (2006).
 On using infrasound from interacting ocean swells for global continuous measurements of winds and temperature in the stratosphere, *J. Geophys. Res.* 111, no. 11, doi: 10.1029/2005JD006690.
- Le Pichon, A., L. Ceranna, C. Pilger, P. Mialle, D. Brown, P. Herry, and N. Brachet (2013). The 2013 Russian fireball largest ever detected by CTBTO infrasound sensors, *Geophys. Res. Lett.* 40, no. 14, 3732–3737.
- Le Pichon, A., R. S. Matoza, N. Brachet, and Y. Cansi (2010). Recent enhancements of the PMCC infrasound signal detector, *InfraMatics*, **26**, 5–8
- Le Pichon, A., V. Maurer, D. Raymond, and O. Hyvernaud (2004). Infrasound from ocean waves observed in Tahiti, *Geophys. Res. Lett.* **31**, no. 19, 2–5.
- Lee, D.-C., J. V. Olson, and C. A. L. Szuberla (2013). Computationally robust and noise resistant numerical detector for the detection of atmospheric infrasound, J. Acoust. Soc. Am. 134, no. 1, 862–868.
- Lyons, J., A. Iezzi, D. Fee, H. Schwaiger, A. Wech, and M. Haney (2020). Infrasound generated by the 2016–2017 shallow submarine eruption of Bogoslof volcano, Alaska, *Bull. Volcanol.* 82, no. 2, doi: 10.1007/s00445-019-1355-0.
- Matoza, R. S., and A. Iezzi, (2022). An infrasound array study of Mount St. Helens, *Dryad*, *Dataset*, doi: 10.25349/D92W38.
- Matoza, R. S., D. Fee, D. N. Green, A. Le Pichon, J. Vergoz, M. M. Haney, T. D. Mikesell, L. Franco, O. A. Valderrama, M. R. Kelley, et al. (2018). Local, regional, and remote seismo-acoustic observations of the April 2015 VEI 4 eruption of Calbuco volcano, Chile, J. Geophys. Res. 123, no. 5, 3814–3827.
- Matoza, R. S., M. A. Garces, B. A. Chouet, L. D'Auria, M. A. Hedlin, C. De Groot-Hedlin, and G. P. Waite (2009). The source of infrasound associated with long-period events at Mount St. Helens, J. Geophys. Res. 114, no. 4, 1–38.
- Matoza, R. S., D. N. Green, A. Le Pichon, P. M. Shearer, D. Fee, P. Mialle, and L. Ceranna (2017). Automated detection and cataloging of global explosive volcanism using the International Monitoring System infrasound network, J. Geophys. Res. 122, no. 4, 2946–2971.
- Matoza, R. S., M. A. Hedlin, and M. A. Garcés (2007). An infrasound array study of Mount St. Helens, *J. Volcanol. Geotherm. Res.* **160**, nos. 3/4, 249–262.
- Matoza, R. S., M. Landès, A. Le Pichon, L. Ceranna, and D. Brown (2013). Coherent ambient infrasound recorded by the International Monitoring System, *Geophys. Res. Lett.* **40**, no. 2, 429–433.
- Mialle, P., D. Brown, and N. Arora (2019). Advances in operational processing at the international data centre, in *Infrasound Monitoring for Atmospheric Studies*, A. Le Pichon, E. Blanc, and A. Hauchecorne (Editors), Springer Nature Switzerland AG, 209–248.
- Montgomery, D. C., E. A. Peck, and G. G. Vining (2001). *Introduction to Linear Regression Analysis*, Third Ed., John Wiley & Sons, Inc., New York.
- Olson, J. V., and C. A. L. Szuberla (2005). Distribution of wave packet sizes in microbarom wave trains observed in Alaska, *J. Acoust. Soc. Am.* **117**, no. 3, 1032–1037.

- Pilger, C., L. Ceranna, J. O. Ross, A. Le Pichon, P. Mialle, and M. A. Garcés (2015). CTBT infrasound network performance to detect the 2013 Russian fireball event, *Geophys. Res. Lett.* 42, 2523–2531.
- Ruigrok, E., S. Gibbons, and K. Wapenaar (2017). Cross-correlation beamforming, *J. Seismol.* **21**, 495–508.
- Schwaiger, H. F., J. J. Lyons, A. M. Iezzi, D. Fee, and M. M. Haney (2020). Evolving infrasound detections from Bogoslof volcano, Alaska: Insights from atmospheric propagation modeling, *Bull. Volcanol.* **82**, no. 3, doi: 10.1007/s00445-020-1360-3.
- Shiro, B. R., M. H. Zoeller, K. Kamibayashi, I. A. Johanson, C. Parcheta, M. R. Patrick, P. Nadeau, L. Lee, and A. Miklius (2021). Monitoring network changes during the 2018 Kilauea volcano eruption, Seismol. Res. Lett. 92, no. 1, 102–118.
- Shumway, R. H. (1971). On detecting a signal in N stationarily correlated noise series, *Technometrics* **13**, no. 3, 499–519.
- Shumway, R. H., S.-E. Kim, and R. R. Blandford (1999). Asymptotics, Nonparametrics and Time Series, in *Chapter Nonlinear Estimation* for Time Series Observed on Arrays, S. Ghosh (Editor), Taylor & Francis Group, Boca Raton, Florida, 227–258.
- Smart, E., and E. A. Flinn (1971). Fast frequency-wavenumber analysis and fisher signal detection in real-time infrasonic array data processing, *Geophys. J. Roy. Astron. Soc.* **26**, nos. 1/4, 279–284.
- Szuberla, C. A. L., and J. V. Olson (2004). Uncertainties associated with parameter estimation in atmospheric infrasound arrays, J. Acoust. Soc. Am. 115, no. 1, 253–258.
- Szuberla, C. A. L., K. M. Arnoult, J. V. Olson, and D. K. Wilson (2006). Discrimination of near-field infrasound sources based on timedifference of arrival information, *J. Acoust. Soc. Am.* 120, no. 3, EL23–EL28.
- Toney, L., D. Fee, K. E. Allstadt, M. M. Haney, and R. S. Matoza (2021). Reconstructing the dynamics of the highly similar May 2016 and June 2019 Iliamna volcano (Alaska) ice-rock avalanches from seismoacoustic data, *Earth Surf. Dynam.* **9**, no. 2, 271–293
- Wilson, C. R., C. A. L. Szuberla, and J. V. Olson (2009). Infrasound monitoring for atmospheric studies, in A. Le Pichon, E. Blanc, and A. Hauchecorne (Editors), *Challenges in Middle Atmosphere Dynamics and Societal Benefits*, Springer, Dordrecht, The Netherlands, 415–454.

Appendix: ParametersData

- Uses data stored locally (miniseed or other common data types) or pulls data from Incorporated Research Institution for Seismology (IRIS)
- SOURCE: Location of stored data [string]
 - 'local': Manually input infrasound data (requires associated station location and metadata)
 - 'IRIS': Uses the University of Alaska Fairbanks (UAF) waveform collection (automatically obtains metadata)
- START: Start time for data processing [UTCDateTime]
- END: End time for data processing [UTCDateTime]

Frequency bands

- Sets total processing frequency limits, number of narrow frequency bands, and allows for frequency band widths to be determined by a few different methods
- FREQ_BAND_TYPE: Frequency band width specification type [string]
 - 'linear': Linear spacing for frequency bands between FMIN and FMAX
 - 'log': Logarithmic spacing for frequency bands between FMIN and FMAX (e.g., Brachet et al., 2010)
 - 'octave': Octave width; upper frequency (*f*2) is twice the lower frequency (*f*1)
 - '2_octave_over': Two octave bands that overlap by 1 octave; upper frequency (*f*2) is 4 times the lower frequency (*f*1) (e.g., Green and Bowers, 2010)
 - 'onethird_octave': One-third octave; the upper band edge (*f*2) is the lower band edge (*f*1) times the cubed root of 2 (e.g., Garces, 2013)
- FMIN: Minimum frequency [float] [Hz]
- FMAX: Maximum frequency [float] [Hz]
- NBANDS: Number of frequency bands [integer]
 - Note: This parameter may get rewritten if using the octave bands, since they put precedence on the FMIN and FMAX values over the number of bands (if they are not in agreement) when creating the narrow frequency band limits

Filters

- Allows for a few different bandpass filter types that can be user specified (uses scipy.signal.iirfilter)
- FILTER_TYPE: Type of filter [string]
 - 'butter': Butterworth filter
 - 'cheby1': Type I Chebyshev filter
- FILTER_ORDER: Order of the filter [integer]

• FILTER_RIPPLE: Filter ripple (only used for cheby1 filter) [float]

Window lengths

- WINOVER: Window overlap [float]; value between 0 and 1
- WINDOW_LENGTH_TYPE: Type of window length [string]
 - 'constant': Single value for all narrow frequency bands
 - 'adaptive': Varies linearly with the period (1/f) (Brachet et al., 2010; Le Pichon et al., 2010)
- WINLEN: Window length [s]; used if WINDOW_ LENGTH_TYPE is constant and 'adaptive' because of the broadband processing plot
- WINLEN_1: Window length for band 1 (lowest frequency)
 [s]; only used if WINDOW_LENGTH_TYPE is 'adaptive'
- WINLEN_X: Window length for band X (the highest frequency) [s]; only used if WINDOW_LENGTH_TYPE is 'adaptive'

Detection

 MDCCM_THRESH: Threshold value of MdCCM for plotting back azimuth and trace velocity results [float]; value between 0 and 1

Miscellaneous

- ALPHA: The percentage of data points to keep in the array processing [float]
 - ALPHA = 1.0: Least-squares processing
 - $0.5 \le ALPHA < 1.0$: Least trimmed squares (LTS) processing

Manuscript received 10 February 2022 Published online 10 June 2022